Letter

# Super Broadband Near-Infrared Phosphors with High Radiant Flux as Future Light Sources for Spectroscopy Applications

Veeramani Rajendran, Mu-Huai Fang, Gabriel Nicolo De Guzman, Tadeusz Lesniewski, Sebastian Mahlik, Marek Grinberg, Grzegorz Leniec, Slawomir Kaczmarek, Yan-Shen Lin, Kuang-Mao Lu, Chih-Min Lin, Ho Chang, Shu-Fen Hu, and Ru-Shi Liu

*ACS Energy Lett.*, **Just Accepted Manuscript** • DOI: 10.1021/acsenergylett.8b01643 • Publication Date (Web): 08 Oct 2018

# Super Broadband Near-Infrared Phosphors with High Radiant Flux as Future Light Sources for Spectroscopy Applications

*Veeramani Rajendran,[†, #] Mu-Huai Fang,[†] Gabriel Nicolo De Guzman,[‡] Tadeusz Lesniewski,[§] Sebastian Mahlik,[§] Marek Grinberg,[§] Grzegorz Leniec,[&] Slawomir M. Kaczmarek,[&], Yan-Shen Lin,[⊥] Kuang-Mao Lu,[⊥] Chih-Min Lin,[⊥] Ho Chang,[*,#] Shu-Fen Hu,[*, ‡] and Ru-Shi Liu[*,†, #]*

†Department of Chemistry, National Taiwan University, Taipei 106, Taiwan

#Department of Mechanical Engineering and Graduate Institute of Manufacturing Technology, National Taipei University of Technology, Taipei 106, Taiwan

‡Department of Physics, National Taiwan Normal University, Taipei 116, Taiwan

§Institute of Experimental Physics, Faculty of Mathematics Physics and Informatics, Gdańsk University, Wita Stwosza 57, 80-308 Gdańsk, Poland

&Institute of Physics, Department of Mechanical Engineering and Mechatronics, West Pomeranian University of Technology Szczecin, al. Piastow 48, 70-311 Szczecin, Poland

⊥Everlight Electronics Co., Ltd., New Taipei City 238, Taiwan

**Corresponding Authors**

* f10381@ntut.edu.tw

* sfhu.hu@ntnu.edu.tw

* rsliu@ntu.edu.tw

## ABSTRACT

The near-infrared (NIR) light source is desirable for real-time non-destructive examination applications, which include the analysis of foodstuffs, health monitoring, iris recognition, and infrared cameras. The emission spectra of such infrared light source should also be broad as possible for effective performance, in view of the broad absorption and reflection of light by the organic elements present in foodstuffs and human health falls in the blue and NIR regions of the electromagnetic spectrum, respectively. In this work, blue light-emitting diode (LED) excitable super broad-band NIR phosphor light source is developed with high FWHM of 330 nm and radiant flux of 18.2 mW for the first time. The observation of super broad-band luminescence from two distinct luminescence centers is studied and evidenced by electron paramagnetic resonance, X-ray absorption near edge structure, steady-state luminescence and time-resolved luminescence at ambient and high-pressure environments. Finally, the luminescence mechanism is discussed with the relevant configurational coordinate diagrams.


## TOC GRAPHICS

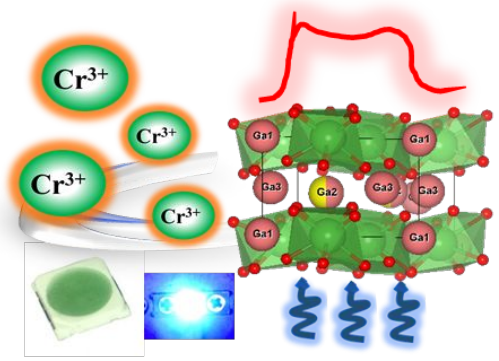

Near-infrared (NIR) light is partly invisible light with a wavelength range of 650 to 1400 nm positioned between the visible and IR regions of the electromagnetic spectrum. NIR spectroscopy uses NIR light as real-time monitoring analytical and non-destructive tool in the food processing industry for detection and composition analysis based on the principle of characteristic light reflection, transmission, and scattering for complex bonds.[1] The NIR light can harmlessly penetrate into human biological tissues at a high attenuation property. The characteristic absorption or scattering by pigmented compounds and tissues present in humans offers the possibility for non-invasive and non-destructive testing in terms of distinguishing tumour tissues and offers biological tissue information. A NIR light source with a broad emission spectrum is needed over the narrow spectra because the wider range of light absorption and reflection spectrum by various organic elements present in foodstuffs and human organs falls at the blue and IR ranges of the electromagnetic spectrum, respectively.[2-3] The commercial light sources available for IR light, notably, tungsten halogen lamp, laser diodes, and supercontinuum lasers, have several disadvantages which including unstable spectral stability, narrow emission spectrum, high electrical consumption, shorter lifetimes than that of light-emitting diode (LED), substantial heat generation, and non-compactness.[4] OSRAM has also demonstrated the prominence of broadband NIR light in the applications of NIR spectroscopy by enabling the IR LED chip that facilitates the mobile phones for analyzing the food composition.[5] In addition, they have also been discussed the perspective of NIR phosphors for endoscopy applications. [6]

Although numerous studies have reported by using rare earth elements ($Pr^{3+}$, $Nd^{3+}$, $Tm^{3+}$, and $Eu^{2+}$) and transitions elements ($Cr^{3+}$, $Ni^{2+}$, $V^{2+}$, and $Mn^{4+}$) for NIR range, however, the emission spectra are not broad as expected and focused for long-persistent luminescence studies.[7-11] The term “radiant flux” or “radiant power” is defined as the amount of radiant energy emerging from the

source per unit time. It is generally described in the units of W, mW or μW which is a characteristic parameter to denote the performance of LED device. The quantum efficiency of the phosphor will determine the radiant flux of the packaged pc-LEDs. Hayashi et al., produced a LED device with an output of 47 mW by combining the $Ce^{3+}$, $Cr^{3+}$-doped $Lu_3Al_5O_{12}$ and $Bi^{2+}$-doped $GeO_2$ amorphous glass for the spectral ranges of 500 nm to 850 nm and 1000 nm to 1600 nm, respectively, with a spectral gap of 900 nm –1000 nm. However, the full width half maximum (*fwhm*) in the NIR range is not as broad as required.[3] Zhang et al., implemented the strategy of disturbing electron orbits by substituting $Cr^{3+}$ in the non-equivalent sites of $Ca_2LuZr_2Al_3O_{12}$:$Cr^{3+}$, $Ce^{3+}$ and covered 750 to 820 nm (*fwhm* = 117 nm) with an output of 2.49 mW, which was only 4.1% superior to that of a tungsten lamp of the same spectral distribution and it is very low.[12] An UV illumination excitable $Cr^{3+}$, M (M = Li, $Pb^{2+}$, $Zn^{2+}$, $Eu^{3+}$, $Tm^{3+}$, and $Dy^{3+}$) doped $La_3Ga_5GeO_{14}$ is reported for long-lasting persistent luminescence application.[13-14] It was again investigated for long-lasting luminescence by changing the co-activators.[15] However, there are no reports explaining the luminescence mechanism with respect to the crystal structure, number of crystallographic sites available for $Cr^{3+}$, and luminescence emerging from different centers. Moreover, the phosphor-converted LED strategy is not studied as an alternative light source for NIR spectroscopy applications with high radiant flux.

In this article, blue LED chip excitable super broad-band $Cr^{3+}$-activated $La_3Ga_5GeO_{14}$ phosphor is developed for NIR luminescence (650 nm to 1200 nm) with *fwhm* of 330 nm. Then, the observance of luminescence from two distinct luminescent centers are explained with respect to the crystal structure, as evidenced by the findings of spectral characterizations at ambient and high-pressure environments. Based on the experimental findings, the luminescence mechanism for $Cr^{3+}$ in two different coordination environments are proposed with the configurational coordinate diagram for

the first time. Finally, the potential of the NIR phosphors is demonstrated through LED packaging with the satisfactorily radiant flux.

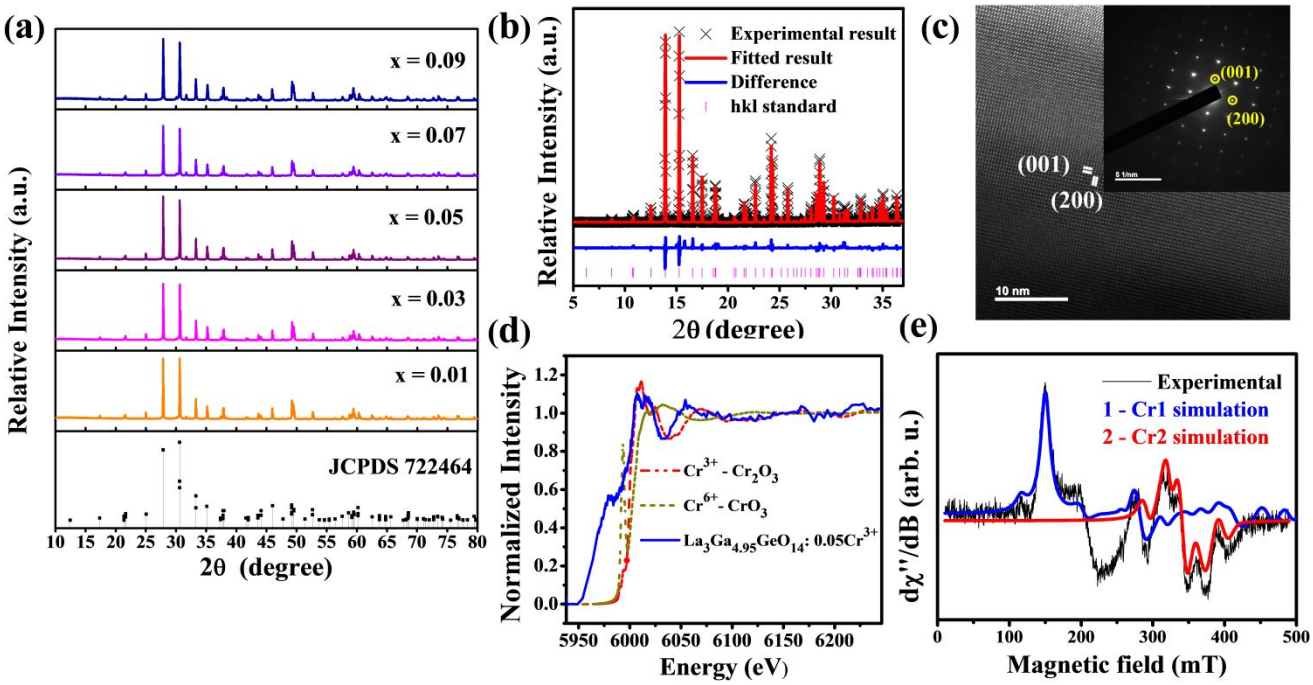


**Figure 1.** a) XRD spectra of $La_3Ga_{5(1-x)}GeO_{14}$: $5xCr^{3+}$ b) Rietveld refinement and c) HRTEM images with SAED pattern of $La_3Ga_{4.95}GeO_{14}$:$0.05Cr^{3+}$. d) XANES spectra of $La_3Ga_{4.95}GeO_{14}$:$0.05Cr^{3+}$ and e) EPR experimental and simulated spectra for two chromium centers: octahedral (1) and tetrahedral (2) sites of $La_3Ga_{4.95}GeO_{14}$:$0.05Cr^{3+}$

The X-ray diffraction (XRD) spectra in Figure 1a reveal that $La_3Ga_{5(1-x)}GeO_{14}$ for the different concentrations of $Cr^{3+}$ has good correlation with the standard JCPDS 722464 except for an impurity peak ($Ga_2O_3$) at 31.6°. The material crystallizes in the space group of P321 (150) of the trigonal crystal system. The crystal system of $La_3Ga_5GeO_{14}$ offers two octahedral $Ga^{3+}$ sites and one tetrahedral $Ga^{3+}$ site for the $Cr^{3+}$ ions to enter into the crystal lattice (Figure S1). The Rietveld refinement results (Figure 1b) also suggest that the samples are synthesized with good crystallinity in a nearly pure phase through the satisfactory refinement values of $\chi 2$, Rwp, and Rp (Table S1).

High-resolution transmission electron microscopy (HRTEM) is conducted to further analyze the structure and crystallinity of the samples along with selected area electron diffraction (SAED) characterizations (Figure 1c). The value of the measured and theoretical interfacial angle is 90°. The measured and theoretical d-spacing values of the (001) plane are 5.07 Å and 5.11 Å, whereas the d-spacing values of the (200) plane are 4.15 Å and 4.10 Å. The closer value of the d-spacing to the refinements results confirms the lack of any superstructure, which further indicates good crystallinity. The elemental mapping of the HRTEM images (Figure S2) confirms the presence and even distribution of the chemical elements in the phosphor. The X-ray absorption near edge structure results (Figure 1d) show that the presence of Cr ions in the tetrahedral sites by the presence of the sharp peak at 5980 eV with a shoulder at 5996.2 eV, whereas the $Cr^{3+}$ ion in the octahedral site is confirmed by the peak at 6003.4 eV similar to that of the standard $Cr_2O_3$.[16] The electron paramagnetic resonance (EPR) in liquid nitrogen temperature (Figure 1e) is also conducted to obtain information on the local coordination symmetry and crystal field environment.[17] The occurrence of a sharp EPR signal centered at $g_{eff}$ ~2 arising from the isolated $Cr^{3+}$ ions (S=3/2) shifts to the lower magnetic field value of $g_{eff}$ ~3.8 due to a large distortion in axial symmetry that affects the splitting of the EPR signal.[18-20] The $La_3Ga_{4.95}GeO_{14}$: $Cr^{3+}$ powder sample exhibits three intense and several weak (up to six lines) while positioned at the chromium (Cr2) ion at the tetrahedral site in weak crystal field. The intense line at the low magnetic field and series of weak lines in a wider range of magnetic field are assigned to the strong crystal field environment of chromium (Cr1) ions. The simulations are performed on the basis of the spin Hamiltonian (SH) equation (refer to the experimental section). Hence, we conclude that the EPR spectra are derived from the two different lattice positions of chromium ions. The calculated values are as follows: 1) octahedral site position: $g^{\parallel} = g^{\perp} = 1.99$, $D = -0.240\ cm^{-1}$, and $E = 0.064\ cm^{-1}$

and 2) tetrahedral site position: g|| = 2.18, $g^{\perp}$ = 1.99, D = − 0.045 $cm^{-1}$, and E = 0 $cm^{-1}$. These results are very close to the parameter values obtained by Prokhorov et al., for chromium-doped single crystals.[21] On the basis of the simulations and experimental results, we integrated EPR intensity for the separate paramagnetic centers and predicts that almost 80% of the chromium ions appear at the octahedral position, whereas only 20% assume the tetrahedral position. The results of temperature analysis of the EPR spectra indicate that the integral intensity fulfils the Curie-Weiss equation with the following Curie-Weiss temperatures: $T_{cw}$ = 4.9 K (octahedral) and $T_{cw}$ = 7.7 K (tetrahedral site). On the basis of SH parameters, we find that the local symmetry for a tetrahedral and octahedral site least $C_4$ and even $C_3$ respectively.

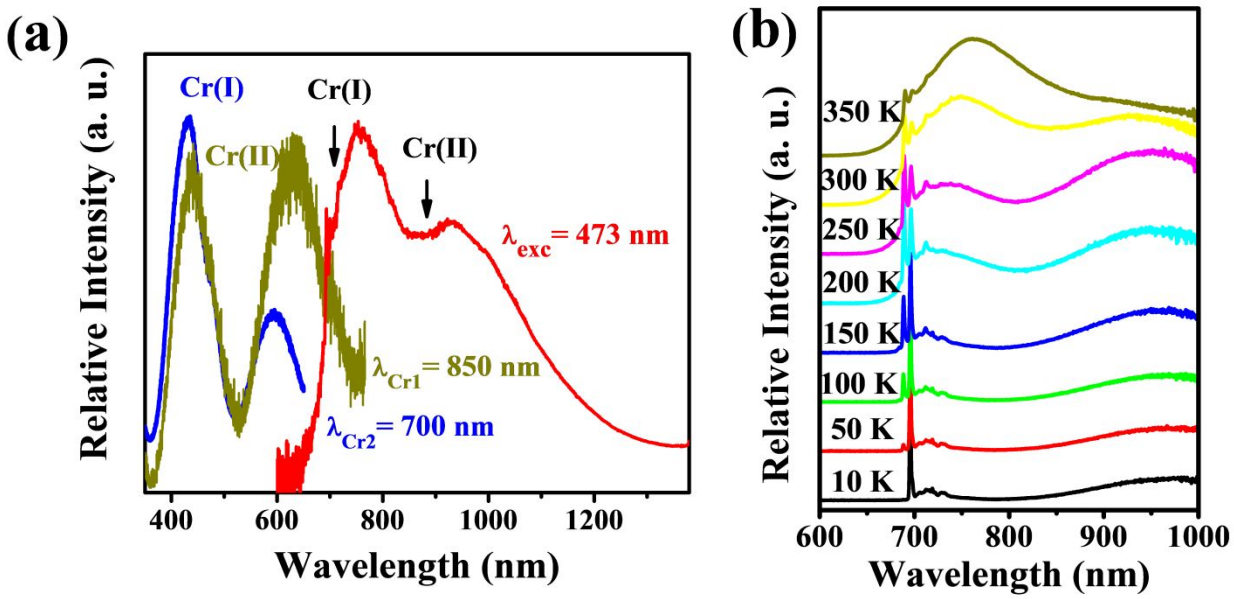


**Figure 2.** a) Photoluminescence spectra and b) Temperature-dependent photoluminescence spectra of $La_3Ga_{4.95}GeO_{14}$: $0.05Cr^{3+}$.

The photoluminescence spectra of $La_3Ga_{4.95}GeO_{14}$:$0.05Cr^{3+}$ (Figure 2a) show the characteristic sharp R-line of $Cr^{3+}$ at 690 nm overlain on the super broadband NIR luminescence emission spectra in the range of 600–1200 nm, with the two distinct luminescence peaking at 750 nm (denoted as

Cr1) and 920 nm (denoted as Cr2) under the excitation wavelength of 473 nm. The sharp R-line (spin-forbidden, $^2E \rightarrow {}^4A_2$) and Cr1 peak (spin-allowed transitions, $^4T_2 \rightarrow {}^4A_2$) suggest the presence of $Cr^{3+}$ ions in the octahedral coordinated environment according to Tanabe-Sugano diagram of $3d^3$ in octahedral configurations (Figure S3). The quantitative description of the $3d^3$ energy structure system (Table S2) gives the intermediate crystal field value of $D_q/B = 2.67$, which agrees well with the observation of both transitions in the same spectra (Figure 1d).[22] The excitation spectra monitored at 750 nm (Cr1) show two strong excitation bands at 595 and 432 nm, attributed to the spin-allowed transitions of $^4A_2 \rightarrow {}^4T_1$ and $^4A_2 \rightarrow {}^4T_2$ respectively. The Cr2 luminescence peak is ascribed to the $Cr^{3+}$ ions in the tetrahedral coordinated environment. The Cr2 peak is assigned to the spin-allowed transition ($^2T_1 \rightarrow {}^4T_1$) of $Cr^{3+}$ in tetrahedral coordination with the respective Tanabe-Sugano diagram of $3d^3$ in tetrahedral coordination (Figure S3) being equivalent to the $d^7$ diagram in octahedral coordination.[23] The corresponding excitation spectra monitored at 920 nm displays two strong excitation bands at 630 and 440 nm similar to Cr1 and attributed to the excited states of $^4T_2$ and $^4A_2$ from the $^4T_1$ ground state, respectively. Notably, the Cr2 excitation spectrum measured at wavelength 850 nm possess an admixture of the emission associated with Cr1. This makes it difficult to clearly determine the energy of the $^4T_1 \rightarrow {}^4T_2$ transition, which strongly overlaps with the Cr1 ($^4A_2 \rightarrow {}^4T_1$) transition in the excitation spectra. Hence, we cannot calculate the energy of the B parameter because the energy of the excited $^4T_2$ state is unknown. However, the difference in the excitation spectra of Cr1 and Cr2 is clearly shown. The optimized concentration of $Cr^{3+}$ is valued as 1% (Figure S4). The obtained low temperature dependent steady-state luminescence spectra (Figure 1d) suggest that the coordination environment of $Cr^{3+}$ determines the luminescence behaviour with respect to the temperature changes from 10 K to 350 K. The Cr1 luminescence changes greatly with temperature, in particular, the temperature increase

leads to the decrease in the intensity of the R-line ($^2E \rightarrow {}^4A_2$) relative to the broadband ($^4T_2 \rightarrow {}^4A_2$). On the contrary, the temperature does not lead to any systematic change of luminescence of the Cr2 centers. The thermal stability of the high-temperature dependent photoluminescence is shown in supporting information Figure S5. The luminescence starts to degrade as a function of increasing temperature however, it possesses good thermal stability of nearly 84% at 473K.

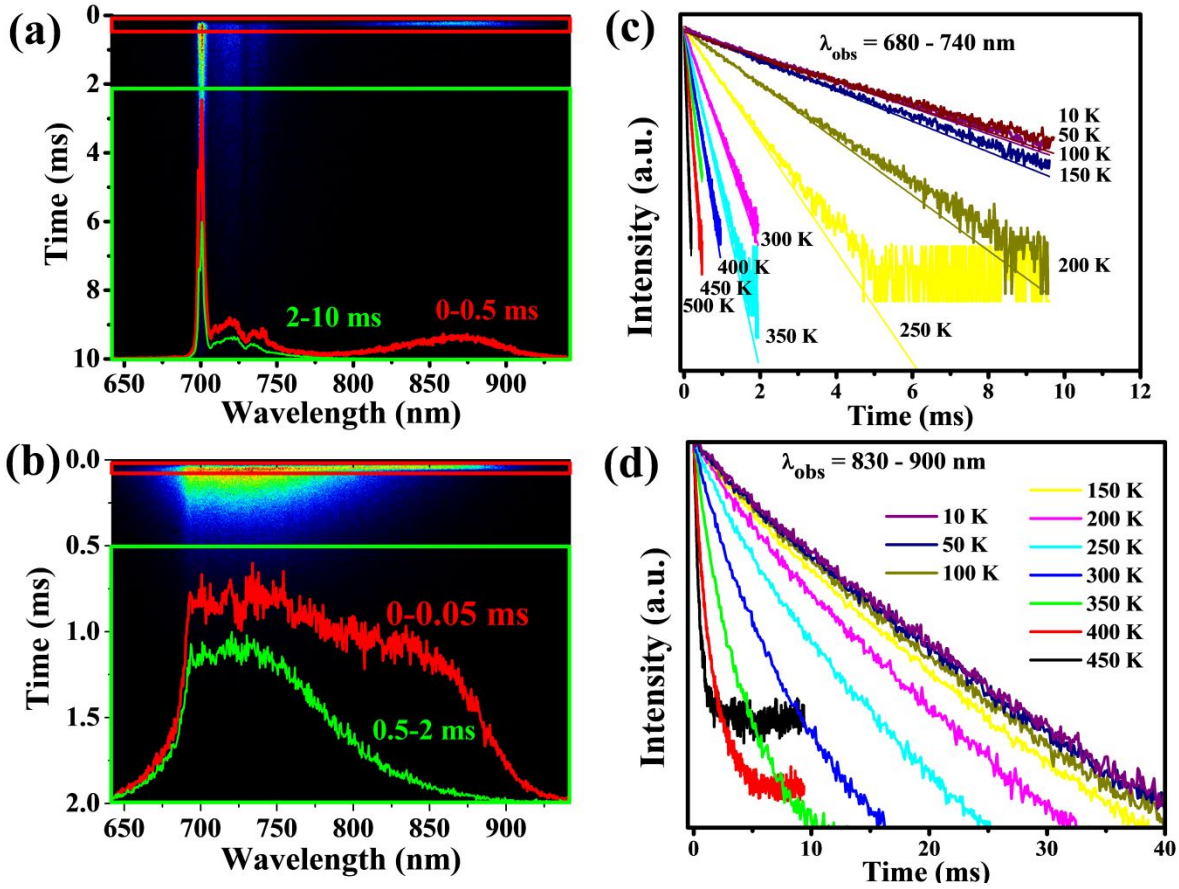


**Figure 3.** TRS in the time range of 0–10 ms and temperatures of (a) 10 K and (b) 300K. The time decay curve of $La_3Ga_{4.95}GeO_{14}$:0.05$Cr^{3+}$ (c) Cr1 (d) Cr2.

The time-resolved luminescence spectra (TRS) at different temperatures are measured for more detailed consideration of the two luminescent centers Cr1 and Cr2. Figure 3a presents the streak camera images of $La_3Ga_{4.95}GeO_{14}$:0.05$Cr^{3+}$ under 440 nm pulse excitation at 10 K, measured in

the time interval 0-10 ms. The Cr1 luminescence consists of R line located at 700 nm accompanied by weak phonon sideband, with decay time in the range of milliseconds. The Cr2 luminescence is present as broadband in the range of 800 – 950 nm with much shorter decay time (microseconds). To illustrate this fact emission spectrum taken at time interval directly after excitation (0-0.5 ms, red box in Figure 3a) were compared to emission spectra taken at time interval of several milliseconds after excitation pulse (2-10 ms, green box in Figure 3a). The emission spectrum directly after excitation (red curve) contains Cr2 emission band centered at 870 nm which is absent in the spectrum take several milliseconds later (green curve). In Figure 3b, a streak image taken at 300 K shows that the R line at room temperature is largely replaced by broad-band Cr1 emission, which is accompanied by a shortening of the decay time. The Cr2 emission remains clearly distinguishable as seen by comparing emission spectra directly after excitation (0-0.1 ms, red curve) with spectrum taken at 0.5-2 ms time interval (green curve). The Cr1 decay profile obtained for a selected temperature between 10 K and 300 K are shown in Figure 3c and fitted by the single exponential equation (Figure S6a). The respective emission spectra are shown in Figure 2a. No obvious change in the decay time of the R-line is noted until the temperature reached 100 K. Thereafter, however, a considerable decrease of the decay ensues with temperature increase which is accompanied by emerging of the broadband emission of Cr1, related to the spin-allowed ($^4T_2 \rightarrow {}^4A_2$) transition. This means that the $^4T_2$ state is located above the lowest excited state $^2E$ and that the occupation of the higher excited $^4T_2$ state is thermally induced with activation energy $\Delta$ equal to the energy difference between $^4T_2$ and $^2E$ state. For $Cr^{3+}$ with an intermediate crystal field value in an octahedral coordinated environment system, the temperature-dependent luminescence lifetime can be approximated by the formula below, where the $^2E$ state is located slightly below the $^4T_2$.[24]

$$\tau = \left[\frac{1 + 3exp\left(-\frac{\Delta}{kT}\right)}{\frac{1}{\tau_E} + \frac{1}{\tau_T}3exp\left(-\frac{\Delta}{kT}\right)}\right] \quad (1)$$

Where $\frac{1}{\tau_E}$ and $\frac{1}{\tau_T}$ are probabilities of radiative transitions $^2E \rightarrow {}^4A_2$ and $^4T_2 \rightarrow {}^4A_2$, respectively. Although the $^2E \rightarrow {}^4A_2$ transition is spin forbidden, it is partly allowed due to the spin-orbit coupling leading to the admixture of the second excited state and the lowest quartet state $^4T_2$ to the $^2E$ state resulting in the following approximate relation between $\frac{1}{\tau_E}$ and $\frac{1}{\tau_T}$: [26-27]

$$\frac{1}{\tau_E} = \frac{1}{\tau_T}\left\{\frac{V_{s-o}}{\Delta'}\right\}^2 \quad (2)$$

Where $V_{s-o}$= effective spin-orbit coupling energy value. Energy Δ' is the energy difference between the $^2E$ and $^4T_2$ states obtained from the excitation spectrum. Energy Δ is smaller than Δ′ by lattice relaxation energy of the system in the $^4T_2$ state, Sħω (refer configurational diagram in Figure S6b).[28] The fitting of temperature-dependent luminescence decay on the basis of eq (1) yields the values $\frac{1}{\tau_E} = 0.39 \cdot 10^6\, s^{-1}$, $\frac{1}{\tau_T} = 2 \times 10^7\, s^{-1}$ and Δ = 490 cm$^{-1}$. It is seen that the formula (1) reproduces the temperature dependence of the luminescence lifetime in the temperature range lower than 250 K. Above 250 K the lifetime diminishes much stronger that it is predicted by the proposed model. To understand this effect, we have modified formula (1) by considering the non-radiative process that is activated with energy $E_{nr}$ and probability $p_{nr}$:

$$\tau = \left[\frac{1 + 3exp\left(-\frac{\Delta}{kT}\right) + exp\left(\frac{-E_{nr}}{kT}\right)}{\frac{1}{\tau_E} + \frac{1}{\tau_T}3exp\left(-\frac{\Delta}{kT}\right) + p_{nr}exp\left(\frac{-E_{nr}}{kT}\right)}\right] \quad (3)$$

Interestingly, the fitted values of the non-radiative decay rate $p_{nr}$ = 2.7 × 10$^7$ s$^{-1}$ and activation energy $E_{nr}$ = 2500 cm$^{-1}$ obtained from fitting are rather small. From the configurational coordinate diagram, it is seen that the value of energy $E_{nr}$ is evidently too small to be interpreted as the energy

of the $^4T_{2g}$ - $^4A_{2g}$ crossing Therefore, the existence of additional quenching state must be considered. The most natural state responsible for luminescence quenching and lifetime reduction in this temperature range is the conduction band (state corresponds to the $Cr^{4+}$ and electron in the conduction band). The Cr2 decay profile obtained for a selected temperature between 10 K and 500 K is shown in Figure 3d. The decays are not single exponential therefore the average luminescence decay time has been calculated using formula.

$$\tau = \frac{\int I(t)tdt}{\int I(t)dt} \qquad (4)$$

Where I(t) is luminescence intensity and presented in Figure S6c. Herein, the ground state is $^4T_1$, and the two excited states are $^2T_2$ and $^4T_2$. The electron-lattice coupling energy is considered to be the same in the $^2T_2$ and $^4T_2$ states and equal to 1800 $cm^{-1}$ (Table S2). Moreover, we consider that excitation to the $^2T_2$ and $^4T_2$ states causes shrinkage and expansion of the lattice, respectively. Therefore, the respective parabolas shift toward opposite directions with respect to the ground electronic manifold. The temperature-dependent luminescence lifetime can be approximated using eq (5) and obtain the values of $\tau$ = 11.5 µs, $E_{nr}$ = 982 $cm^{-1}$, and $p_{nr}$ = 1.6107 $s^{-1}$ (refer configurational coordinate diagram in Figure S6d).

$$\tau = \left[\frac{1 + exp\left(\frac{-E_{nr}}{kT}\right)}{\frac{1}{\tau_0} + + p_{nr} exp\left(\frac{-E_{nr}}{kT}\right)}\right] \qquad (5)$$

The fitting curves seem unconvincing. Therefore, we assume two possible channels of the non-radiative de-excitation with the modified formula below:

$$\tau = \left[\frac{1 + exp\left(\frac{-E_{nr}}{kT}\right) + exp\left(\frac{-E_{nr1}}{kT}\right)}{\frac{1}{\tau_0} + p_{nr1} exp\left(\frac{-E_{nr1}}{kT}\right) + p_{nr2} exp\left(\frac{-E_{nr2}}{kT}\right)}\right] \qquad (6)$$

The best fit is obtained for $\tau$ = 11.5 µs, $p_{nr1} = 0.34 \cdot 10^6\, s^{-1}$, $p_{nr2} = 7.33 \cdot 10^8\, s^{-1}$, $E_{nr1}$ = 275 $cm^{-1}$, and $E_{nr2}$ = 1732 $cm^{-1}$. We propose that the non-radiative de-excitation is related to the auto ionization of the $Cr^{3+}$ to the conduction band. The small value of $p_{nr}$ or $p_{nr1}$may be related to the large value of Huang-Rhys parameter $S_{Cr^{4+}}$, which is greater for chromium in the tetrahedral coordination than in the octahedral coordination. The nature of the second state, which is activated with the energy $E_{nr2}$ = 1732 $cm^{-1}$, is unclear. It can be tentatively attributed to the crossing of the $^4T_1$ and $Cr^{4+}$ +e electronic manifold, which causes direct relaxation of the electron from the conduction band to the $^4T_1$ state, or excitation of the system to the higher vibrionic levels of the $Cr^{4+}$ + e electronic manifold, which is more probable due to the fact that $|F^{0i}|^2 \gg |F^{00}|^2$ for $i = \frac{E_{nr2} - E_{nr1}}{\hbar\omega}$. The luminescence spectra of $La_3Ga_{4.95}GeO_{14}$: $0.05Cr^{3+}$ obtained at different pressures and at room temperature are presented and discussed in supporting information (Figure S7 and Figure S8).

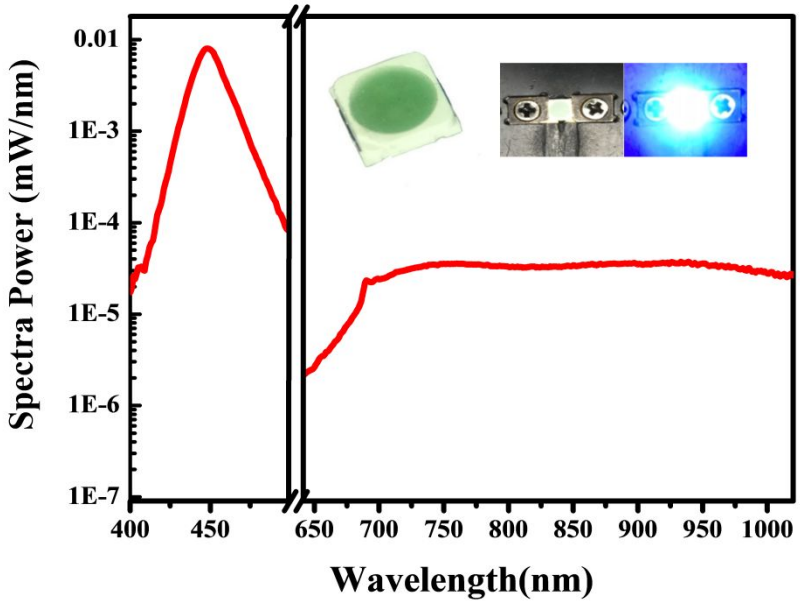

**Figure 4.** The LED packaging results of $La_3Ga_{4.95}GeO_{14}$:$0.05Cr^{3+}$ (The inset in the figure shows packaged LED chip and mounted LED device in operation).

The pc-LED device is fabricated by using the blue LED chip (450 nm) for excitation, $La_3Ga_{4.95}GeO_{14}$: $0.05Cr^{3+}$ as the conversion element and silicon as a binder. The higher radiant flux of 18.2 mW is obtained in the spectral range of 650 nm to 1050 nm by operating at an input electric current of 350 mA. The photoelectric energy conversion efficiency is computed as 76.59 %. The LED packing results seem more satisfactorily for broadband related near-infrared applications as compared to conventional phosphors. Finally, the luminescence mechanisms are proposed based on the results of luminescence studies at ambient and high-pressure environments in addition to the time-resolved luminescence studies. These works opens an opportunity to design the broadband NIR phosphors with a clear background. We hope this works will encourage more researchers to develop other possible phosphors system for broadband NIR phosphors. Future works are particularly focused in the chemical tuning of the host for more effective radiant flux

ASSOCIATED CONTENT

**Supporting Information**. The Supporting Information is available free of charge on the ACS Publications website at DOI: XXXX. Experimental Section includes synthesis of $La_3Ga_{5(1-x)}GeO_{14}$: $5xCr^{3+}$ and details of characterization techniques. The HRTEM elemental mapping, crystal structure; photoluminescence; Tanabe-Sugano diagrams of $d^3$ and $d^7$ systems; time-resolved spectroscopy decay curves with fitting; pressure-dependent luminescent properties with relevant decay curve fitting; refined crystallographic data; quantitative description of $Cr^{3+}$ centers.

AUTHOR INFORMATION

The authors declare no financial competing interest.

ACKNOWLEDGEMENTS

This work was supported by the Ministry of Science and Technology of Taiwan (contract nos. MOST 107-2113-M-002-008-MY3 and MOST 106-2112-M-003-007-MY3) and the National Center for Research and Development Poland Grant (No. PL-TW/V/1/2018).

REFERENCES

(1) Guelpa, A.; Marini, F.; du Plessis, A.; Slabbert, R.; Manley, M. Verification of Authenticity and Fraud Detection in South African Honey Using NIR Spectroscopy. *Food Control* **2017,** *73*, 1388 1396.

(2) Ye, M.; Gao, Z.; Li, Z.; Yuan, Y.; Yue, T. Rapid Detection of Volatile Compounds in Apple Wines Using FT-NIR Spectroscopy. *Food Chem.* **2016,** *190*, 701 708.

(3) Hayashi, D.; Dongen, A. M. V.; Boerekamp, J.; Spoor, S.; Lucassen, G.; Schleipen, J. A Broadband LED Source in Visible to Short-Wave-Infrared Wavelengths for Spectral Tumor Diagnostics. *Appl. Phys. Lett.* **2017,** *110*, 233701.

(4) Evers, D. J.; Nachabé, R.; Klomp, H. M.; van Sandick, J. W.; Wouters, M. W.; Lucassen, G. W.; Hendriks, B. H. W.; Wesseling, J.; Ruers, T. J. M. Diffuse Reflectance Spectroscopy: A New Guidance Tool for Improvement of Biopsy Procedures in Lung Malignancies. *Clin. Lung Cancer* **2012,** *13*, 424 431.

(5) Halper, M. **(2018)**. Osram's Latest Infrared LED Identifies What's in Your Food (UPDATED). [online] Ledsmagazine.com. Available at:

https://www.ledsmagazine.com/articles/2018/09/osram-s-latest-infrared-led-identifies-what-s-in-your-food.html [Accessed 21 Sep. 2018].

(6) Tragl, S.; Eisert, D.; Lange, S.; Kaufmann, N.; Martin, A.; Bergenek, K. Radiation-Emitting Optoelectronic Component. WIPO. Appl. No. PCT/EP2016/059672, April, 2016.

(7) Zhuang, Y.; Katayama, Y.; Ueda, J.; Tanabe, S. A Brief Review on Red to Near-Infrared Persistent Luminescence in Transition-Metal-Activated Phosphors. *Opt. Mater.* **2014,** *36*, 1907 1912.

(8) Kaminskii, A. A.; Shkadarevich, A. P.; Mill, B. V.; Koptev, V. G.; Demidovich, A. A. Wide-Band Tunable Stimulated Emission from a $La_3Ga_5SiO_{14}$-$Cr^{3+}$ Crystal. *Inorg. Mater.* **1987,** *23*, 618 619.

(9) Zabiliūtė, A.; Butkutė, S.; Žukauskas, A.; Vitta, P.; Kareiva, A. Sol-Gel Synthesized Far-Red Chromium-Doped Garnet Phosphors for Phosphor-Conversion Light-Emitting Diodes that Meet the Photomorphogenetic Needs of Plants. *Appl. Opt.* **2014**, *53*, 907.

(10) Gao, Z.; Liu, Y.; Ren, J.; Fang, Z.; Lu, X.; Lewis, E.; Farrell, G.; Yang, J.; Wang, P. Selective Doping of $Ni^{2+}$ in Highly Transparent Glass-Ceramics Containing Nano-Spinels $ZnGa_2O_4$ and $Zn_{1+x}Ga_{2-2x}Ge_xO_4$ for Broadband Near-Infrared Fiber Amplifiers. *Sci. Reports.* **2017**, *7*, 1783.

(11) Zhang, L.; Zhang, S.; Hao, Z.; Zhang, X.; Pan, G.-H.; Luo, Y.; Wu, H.; Zhang, J. A High Efficiency Broad-Band Near-Infrared $Ca_2LuZr_2A_3O_{12}$:$Cr^{3+}$ Garnet Phosphor for Blue LED Chips. *J. Mater. Chem. C* **2018,** *6*, 4967 4976.

(12) Zhang, S.; Hu, Y.; Duan, H.; Chen, L.; Fu, Y.; Ju, G.; Wang, T.; He, M. Novel $La_3GaGe_5O_{16}$ : $Mn^{4+}$ Based Deep Red Phosphor: A Potential Color Converter for Warm White Light. *RSC Adv.* **2015**, *5*, 90499 90507.

(13) Yan, W.; Liu, F.; Lu, Y.-Y.; Wang, X.-J.; Yin, M.; Pan, Z. Near Infrared Long-Persistent Phosphorescence in $La_3Ga_5GeO_{14}$:$Cr^{3+}$ Phosphor. *Opt. Express* **2010,** *18*, 20215 20221.

(14) Jia, D.; Lewis, L. A.; Wang, X.-J. $Cr^{3+}$-Doped Lanthanum Gallogermanate Phosphors with Long Persistent IR Emission. *Electrochem. Solid-State Lett.* **2010**, *13,* J32 J34.

(15) Wu, Y.; Li, Y.; Qin, X.; Chen, R.; Wu, D.; Liu, S.; Qiu, J. Dual Mode NIR Long Persistent Phosphorescence and NIR-to-NIR Stokes Luminescence in $La_3Ga_5GeO_{14}$: $Cr^{3+}$, $Nd^{3+}$ Phosphor. *J. Alloys Compd.* **2015,** *649*, 62 66.

(16) Pantelouris, A.; Modrow, H.; Pantelouris, M.; Hormes, J.; Reinen, D. The Influence of Coordination Geometry and Valency on the K-edge Absorption Near Edge Spectra of Selected Chromium Compounds. *Chem. Phys.* **2004,** *300*, 13 22.

(17) Kaczmarek, S. M.; Leniec, G.; Fuks, H.; Skibiński, T.; Pelczarska, A.; Godlewska, P.; Hanuza, J.; Szczygieł, I. Magnetic Characterization of Microcrystalline $Na_3Ln_{0.99-X}Er_{0.01}Cr_x(PO_4)_2$ Orthophosphates Synthesized by Pechini Method (Ln = La, Gd). *World J. App. Phys.* **2017,** *2*, 7 18.

(18) Li, Y.; Ye, S.; Zhang, Q. Ultra-Broadband Near-Infrared Luminescence of Ordered-Disordered Multi-Sited $Cr^{3+}$ in $La_3Ga_{5.5}Nb_{0.5}O_{14}$: $Cr^{3+}$. *J. Mater. Chem. C* **2014,** *2*, 4636 4641.

(19) De Vicente, F. S.; Santos, F. A.; Simões, B. S.; Dias, S. T.; Siu Li, M. EPR, Optical Absorption and Luminescence Studies of $Cr^{3+}$-doped Antimony Phosphate Glasses. *Opt. Mater.* **2014,** *38*, 119 125.

(20) Grachev, V.; Malovichko, G. EPR, ENDOR, and Optical-Absorption Study of $Cr^{3+}$ Centers Substituting for Niobium in Li-Rich Lithium Niobate Crystals. *Phys. Rev. B* **2000,** *62*, 7779 7790.

(21) Prokhorov, A. A. Static and Dynamic Characteristics of the $Cr^{3+}$ EPR Spectra in the Van Vleck Paramagnet $TmAl_3(BO_3)_4$. *J. Mater. Sci.* **2016,** *51*, 4762 4768.

(22) Tanabe, Y.; Sugano, S. On the Absorption Spectra of Complex Ions. I. *J. Phys. Soc. Jpn.* **1954,** *9*, 753 756.

(23) Reisfeld, M. J.; Matwiyoff, N. A.; Asprey, L. B. The Electronic Spectrum of Cesium Hexafluoromanganese (IV). *J. Mol. Spectrosc.* **1971,** *39*, 8 20.

(24) Kamińska, A.; Kaczor, P.; Durygin, A.; Suchocki, A.; Grinberg, M. Low-Temperature High-Pressure Spectroscopy of Lanthanum Lutetium Gallium Garnet Crystals Doped with $Cr^{3+}$ and $Nd^{3+}$. *Phys. Rev. B* **2002,** *65*, 104106.

(25) Galanciak, D.; Perlin, P.; Grinberg, M.; Suchocki, A. High Pressure Spectroscopy of LLGG Doped with $Cr^{3+}$. *J. Lumin.* **1994,** *60-61*, 223 226.

(26) Grinberg, M.; Suchocki, A. Pressure-Induced Changes in the Energetic Structure of the $3d^3$ Ions in Solid Matrices. *J. Lumin.* **2007,** *125*, 97 103.

(27) Wu, W.-L.; Fang, M.-H.; Zhou, W.; Lesniewski, T.; Mahlik, S.; Grinberg, M.; Brik, M. G.; Sheu, H.-S.; Cheng, B.-M.; Wang, J.; Liu, R. S. High Color Rendering Index of $Rb_2GeF_6$: $Mn^{4+}$ for Light-Emitting Diodes. *Chem. Mater.* **2017,** *29*, 935 939.

(28) Grinberg, M.; Lesniewski, T.; Mahlik, S.; Liu, R. S. $3d^3$ System–Comparison of $Mn^{4+}$ and $Cr^{3+}$ in Different Lattices. *Opt. Mater.* **2017,** *74*, 93 103.